Influence of High-Power Electric Motor on an FPGA used in the Drive System of Electric Car

Marc Alexandre Kacou*+, Fakhreddine Ghaffari+, Olivier Romain+, Bruno Condamin*
* VALEO, VALEO Powertrain System, Product Electronic Line, Cergy-Pontoise, France
Email : {marc.kacou, bruno.condamin}@valeo.com
+ ETIS, UMR 8051 / ENSEA, University of Cergy-Pontoise, CNRS, F-95000, Cergy-Pontoise, France
Email : {assi-marc.kacou, fakhreddine.ghaffari, olivier.romain}@ensea.fr

***Abstract*—This paper presents an empirical method to model the impact of industrial harsh electromagnetic environment on a Field-Programmable Gate Array (FPGA). The methodology focuses principally on the magnetic field effects and is based on three phases: first, an assessment of the radiated magnetic field of the considered source is performed by measurements or by simulations based on Finite Element Method (FEM). Then, the sensitivity of the FPGA to radiated magnetic field is experimentally evaluated. Finally, by combining these results, a parametric model characterizing the effects of a magnetic field on an FPGA is established. This model can then be integrated into a CAD tool in order to take these effects into account at the design stage of the FPGA-based system. This method is applied to investigate the effects of an electric car's high-power electric motor on its control system implemented in FPGA.**

***Keywords*—Field Programmable Gate Array (FPGA), Electromagnetic Interference (EMI), synchronous motor, electric vehicle, motor stray magnetic field.**

I. Introduction

The industry's interest for FPGAs is growing year after year due to their low cost, a fast time-to-market and their ability to be easily reconfigurable. In applications such as electric motor control, where Digital Signal Processors (DSP) and microcontrollers are widely used, FPGAs offer several advantages that could pave the way for a more prominent role. Unlike microcontrollers and DSP which execute tasks sequentially, an FPGA can efficiently parallelize time consuming tasks, leading to a faster execution time. For instance, in [1], the FPGA implementation of a control algorithm is twenty-five times faster than the DSP-based solution. On another hand, FPGAs offer a very low latency in the execution of control algorithms as there is no extra-latency due to interrupts processing like in DSPs and microcontrollers, allowing a finer control of the electric motor. Another limitation of DSPs and microcontrollers over FPGA is the fixed amount of built-in blocks. In [2], the authors had to implement a multilevel space vector modulation requiring the simultaneous control of twelve switches but could not find a cheap DSP with enough pulse-width modulation (PWM) blocks and overcame this limitation by using a low-cost FPGA. Thereby, over the last few years, FPGAs began to be used in electric motor control applications by replacing or assisting DSPs and microcontrollers, enabling the implementation of novel and more efficient motor control processes [3], [4], [5]. In the automotive industry, especially in the electric vehicle field, FPGAs are also intended to be used as related constraints like vehicle autonomy, passengers comfort and safety, require a precise and high-performance control of the electric motor [6], [7]. That trend will be amplified as modern FPGAs offer more computational power by integrating more features on-chip while reducing the associated power consumption, thanks to the use of advanced fabrication processes.

With technology downscaling, components become more subject to environmental disturbances. In an electric vehicle, the use of high-power electric motors to propel the car induces a under-hood harsh electromagnetic environment in addition to common environmental parameters such as temperature and ionizing radiation. For an electric vehicle, it is of paramount importance to ensure the correct execution of the control algorithm as a defect can lead to dramatic consequences. The effects of temperature and ionizing radiation on FPGAs are well described in the literature [8], [9], but, to the best of our knowledge, there is no published work dealing with the effects of a motor magnetic field on an FPGA. In that sense, we propose an empirical methodology to determine the effects of a magnetic field on an FPGA. This methodology can then be used to determine the effect of any electric motor on any FPGA. Being aware of the effects of a magnetic field source on an FPGA will help FPGA-based system designers to anticipate the corresponding problems at the design phase and apply the required countermeasures.

We present the methodology as well as its application to an electric motor in the following paragraphs of this paper. Section II presents the proposed methodology in details and section III, its application to a high-power electric motor, from the analysis of the FPGA magnetic sensitivity in subsection III-A to the effects on the FPGA presented in subsection III-C via the analysis of the motor radiated magnetic field described in subsection III-B.

II. Methodology

The proposed methodology, presented in Fig. 1, is based on three phases: the FPGA sensitivity to magnetic field is measured, an assessment of the surrounding magnetic field is performed and finally, by combining these two results, the effect of the magnetic field on the FPGA can be evaluated.

978-1-5090-3474-1/16/$31.00 ©2016 IEEE

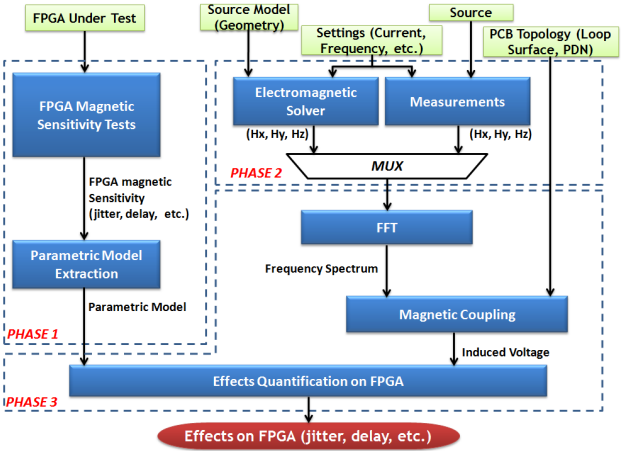

Fig. 1. From magnetic field to effects on the FPGA, the different phases of the proposed methodology.

The first phase consists in determining the magnetic sensitivity of the FPGA which is the quantification of the deviation in the FPGA operation when exposed to a magnetic field. Considering a given loop and Maxwell-Faraday equation given by equation (1) which can be rewritten for a single frequency magnetic field as equation (2) when the loop is electrically small, we can compute the induced voltage from a given magnetic field. $V_{emi}(t)$ is the time domain induced voltage from the magnetic field, F the frequency of that magnetic field, μ_0 the permeability of free space, S the area of the considered loop and H_n, the corresponding quantity of the magnetic field perpendicular to that loop. For a multi-frequency field, equation (2) can be extended to equation (3) where $V_{emi_N}(t)$ is the time domain induced voltage from the multi-frequency magnetic field, N the number of harmonics of the magnetic field, F_i the frequency associated to a given harmonic and $H_n(F_i)$, the corresponding quantity of the magnetic field associated to that harmonic, perpendicular to the loop.

$$\oint_{\partial S} E \cdot dl = -\iint_{S} \frac{\partial B}{\partial t} \cdot dS \tag{1}$$

$$V_{emi}(t) = 2.\pi.F.\mu_0.H_n.S\ sin(2\pi Ft) \tag{2}$$

$$V_{emi_N}(t) = \sum_{i=1}^{N} 2.\pi.F_i.\mu_0.H_n(F_i).S\ sin(2\pi F_i t) \tag{3}$$

These equations state that, for a given magnetic field magnitude, the greater the loop surface or the magnetic field frequency, the higher the induced voltage will be. Hence, at the die scale and for a low frequency magnetic field, it can be easily anticipated that the resulting induced voltage will be negligible due to the micrometric size of the on-die connections. In this case, the magnetic field will impact the FPGA indirectly, more precisely by coupling on the FPGA power supply lines as described in Fig. 2. In this case, the considered loop is the one formed by the FPGA power supply lines. The Power Distribution Network (PDN) includes all components and stray elements in the path of the power supply

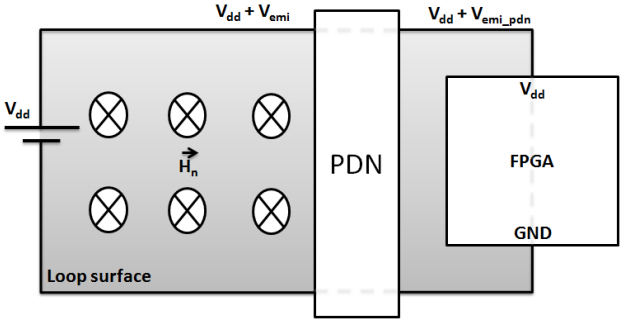

Fig. 2. Magnetic coupling on FPGA power supply lines.

lines on the printed circuit board (PCB) such as decoupling capacitors, PCB stray inductance, etc. Accordingly, when considering a low frequency magnetic field source such as an electric motor, the magnetic sensitivity tests boil down to measure the effects of power supply voltage variation on the FPGA. These tests will give for any FPGA, its defect models representing the variation of the observed defects as a function of the applied voltage, image of a particular magnetic field strength.

The second phase consists in determining the strength of the surrounding magnetic field. This can be done by measurements or by relying on an electromagnetic solver using a model of the considered source. A worst case analysis is performed by measuring or simulating the magnetic field radiated by the source when generating its highest radiated magnetic field.

In the last phase, the frequency spectrum of the measured or simulated magnetic field is obtained by performing a Fast Fourier Transform (FFT) and will then be used as an input to equation (3) to determine the induced voltage resulting from the magnetic field coupling on the FPGA power supply lines. Then, the transfer function of the PDN is applied to the induced voltage to deduce the effect of the PDN on the coupling voltage. Finally, the effect of the magnetic field source on the FPGA is determined by mapping the resulting induced voltage after the PDN on the FPGA parametric model, giving the induced defects from the considered magnetic field source and PCB topology.

III. Application to a High-Power Electric Motor

A. Phase 1 - FPGA Magnetic Sensitivity

As the considered magnetic field source is an electric motor, it will generate a low frequency magnetic field. Hence, the effect of a magnetic field coupling on the power supply lines of the FPGA is considered as a low frequency magnetic field will not directly affect the FPGA as previously explained. In order to measure the FPGA sensitivity to a magnetic field, the test board presented in Fig. 3 has been designed in a specific manner allowing a direct access to the different FPGA power supply pins. The supply voltage can then be varied and the measurement of the corresponding effects on the FPGA can be done.

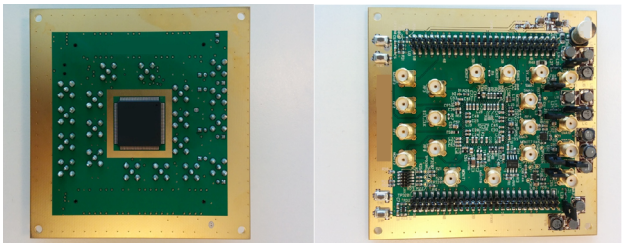

Fig. 3. FPGA test board. Top (left) Bottom (right).

Inside an FPGA, there is a network of highly configurable cells, commonly called Configurable Logic Blocks (CLB). Each basic CLB contains at least one Look-Up Table (LUT), able to implement any combinatorial logic function and one D-type Flip-Flop to implement any sequential logic function. In this paper, only the effects on the LUT propagation delay is considered. From [10], a first order analysis of the relation linking the power supply voltage to the propagation delay for an inverting gate is expressed as:

$$T_{plh} = \frac{C_L \left[\frac{2|V_{th,p}|}{V_{dd}-|V_{th,p}|} + ln\left(3 - 4\frac{|V_{th,p}|}{V_{dd}}\right)\right]}{\mu_p C_{ox} \frac{W_p}{L_p} \left(V_{dd} - |V_{th,p}|\right)} \quad (4)$$

where T_{plh} is the propagation delay from logic low to logic high, V_{dd}, the power supply voltage, $V_{th,p}$ the PMOS threshold voltage, C_L the load capacitance, μ_p the holes mobility, C_{ox} the gate oxide capacitance and (W_p/L_p) the aspect ratio of the PMOS. For T_{phl}, the propagation delay from logic high to logic low, the formula is the same except that the PMOS parameters should be replaced by the NMOS ones. From that equation, we can observe that the propagation delay in digital CMOS circuits is inversely proportional to the supply voltage. Note also that due to that inverse variation, the power supply voltage reduction leads to higher delay variation than its increase.

The nominal power supply voltage of the FPGA under test is rated at 1.2 V and an internal mechanism monitors this voltage. As soon as it goes below a trip point, the FPGA freezes until the voltage goes back to an acceptable level and then restarts. That trip point has been measured at approximately 0.8 V to 0.825 V. The delay variation of the FPGA has been measured from 0.85 V to 1.6 V with the design presented in Fig. 4. As the CLBs inside the FPGA on the board are clustered into 1395 groups, the test design consists in a square wave feeding

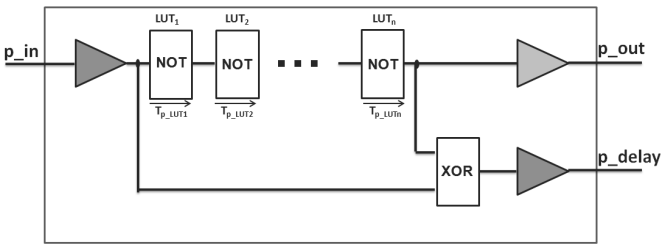

Fig. 4. FPGA design used to measure the propagation delay variation.

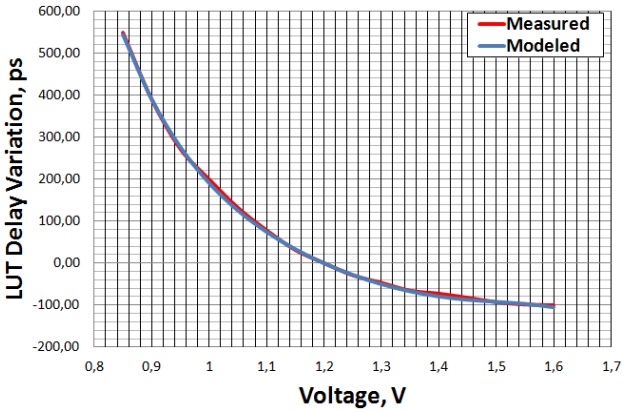

Fig. 5. One LUT delay variation.

a chain of 1394 LUTs implementing inverting logic gates. The delay is measured by another LUT implementing a XOR gate which will have its output high as long as the chain output logic level differs from the input one. Each LUT is mapped to a CLB cluster, resulting in the chain being uniformly distributed throughout the FPGA surface to take into account the on-chip variation effects [11]. Fig. 5 presents the measured delay variation of one LUT and exhibits the delay inverse variation in respect to the supply voltage.

From that analysis, a linear parametric model (5) representing the delay variation of the LUT as a function of the variation of the supply voltage has been extracted, with the parameters given in Table I.

$$\Delta T_P(\Delta V) = \sum_{i=1}^{5} c_i . \Delta V^i, for \ -0.35V \leq \Delta V \leq 0.4V \quad (5)$$

ΔT_P is the propagation delay variation in picoseconds and ΔV is the variation of the power supply in volts. This model will then be used to determine the effect of the motor stray magnetic field on the FPGA.

TABLE I
FPGA MODEL PARAMETERS

c_1	-608.37	c_4	5157.46
c_2	1194.11	c_5	-10127.33
c_3	-1261.43		

B. Phase II - Electric Motor Radiated Magnetic Field

For this study, the modeling and magnetic simulation of the 2004 Toyota Prius electric motor have been considered. This motor has a relatively simple and easy-to-model geometry and has been deeply analyzed by the Oak-Ridge National Laboratory (ORNL) through several reports [12], [13], giving enough data to model it with good accuracy. The motor is a 50 kW, three-phase interior permanent magnet synchronous motor (I-PMSM) with a maximum rated speed of 6000 rpm. The characteristics of the motor are given in Table II.

Before explaining the simulation of the motor, it is important to understand the origin of the radiated magnetic field. For

TABLE II
2004 TOYOTA PRIUS MOTOR PARAMETERS

Parameters	Details
No. of phases	3
No. of poles	8
No. of stator slots	48
No. coils per phase	8
Slots per pole per phase	2
Max. Torque	400 Nm
Max. Speed	6000 rpm
Base Speed	1193 rpm
Max. Voltage	500 Volts
Max. Current	250 Amps
Max. Power	50 kW

the rotation, a magnetic field has to be created on the stator and the rotor parts of the motor, with the stator magnetic field pulling the rotor one. In the case of a three-phase PMSM, the rotor magnetic field (B_{rotor}) is constant and is obtained using high-strength permanent magnets while the rotating magnetic field on the stator (B_{stator}) is created by supplying a three-phase current to the stator windings. That three-phase current is elaborated in a specific manner, depending on the rotor position, to create a rotating magnetic field on the stator resulting in the rotation of the rotor. In an electric car, this is done by an inverter converting the DC voltage from the battery into the required 3-phase current depending on the driver solicitations. The resulting torque allows a vehicle to move and is controlled, for a PMSM, by equation (6a) where T_{syn} is the synchronous torque from the permanent magnets and T_{rel}, the reluctance torque from the rotor geometry. T_{syn} and T_{rel} are given by equations (6b) and (6c) where pp is the motor number of pole pairs, I_d, the current in the direct axis (d-axis) which is the axis of the rotor magnetic field, I_q, the current in the quadrature axis (q-axis) which is the axis perpendicular to the rotor one, ϕ_m, the magnetic flux from the permanent magnets, L_d and L_q, respectively the inductance of the d-axis and q-axis as reported in Fig. 6. I_d and I_q are linked by equation (7) where I_{smax} is the stator maximal current.

$$T_{em} = T_{syn} + T_{rel} \tag{6a}$$
$$T_{syn} = pp.I_q.\phi_m \tag{6b}$$
$$T_{rel} = pp.I_q.I_d.(L_d - L_q) \tag{6c}$$

$$I_{smax} \geq \sqrt{{I_d}^2 + {I_q}^2} \tag{7}$$

For a non-salient pole machine, the reluctance torque is equal to zero as L_d and L_q are equals, whereas for salient pole machines, L_d is commonly less than L_q. Thus, as pp is always positive as well as I_q for motoring operation, a positive reluctance torque is obtained when performing rotor field weakening by applying a negative d-axis current. As the magnetic field radiated by the motor is the sum of the rotor and stator magnetic fields, it will be maximal when B_{rotor} and B_{stator} are maximized. That configuration is obtained by applying no current on d-axis, leading to a maximal rotor

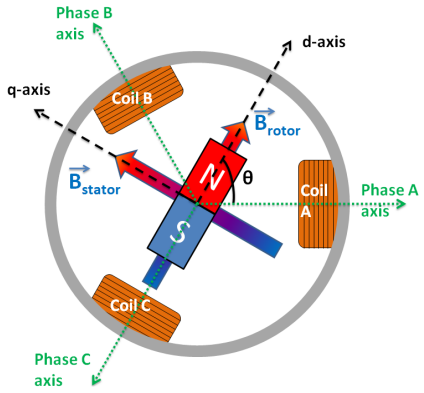

Fig. 6. Magnetic fields inside a two-pole PMSM.

magnetic field while applying the maximal current on q-axis, leading to a maximal stator magnetic field. These magnetic fields might not be limited to the motor housing and could propagate outside, constituting the motor stray magnetic field [14].

To simulate this motor and extract its maximal radiated magnetic field, the open source 2D electromagnetic solver, Finite Element Method Magnetics (FEMM) [15], has been used. It is important to note that due to the 2D modeling, the stator windings outside the stator core, are not simulated, leading to a computed magnetic field less than the one that should be measured on the real motor, but gives a basis to this study. The model has first been validated by simulating the torque in respect to the rotor angle and comparing it to the measured one given in [13]. The result is presented in Fig. 7 and shows that the model is close to the real motor. The differences can be accounted to the generic materials selected in the model as we did not have the full properties of the real motor materials.

To determine the highest possible motor radiated field that the FPGA will face, a worst case analysis has been performed. It consisted in simulating the motor when I_d is set to zero while I_q is set to the motor maximal current as previously explained. The motor base speed has also been considered as it is the highest speed at which the motor can operate without field weakening, hence the highest frequency at which the motor magnetic field is maximum. As the FPGA is on a board inside the inverter, the inverter geometry has been considered. It has been represented as a 5-mm-thick aluminum rectangle. A worst case vehicle integration has also been considered

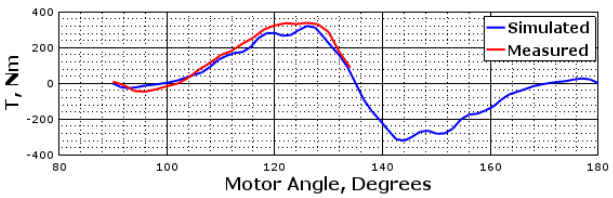

Fig. 7. Measured and simulated torque comparison.

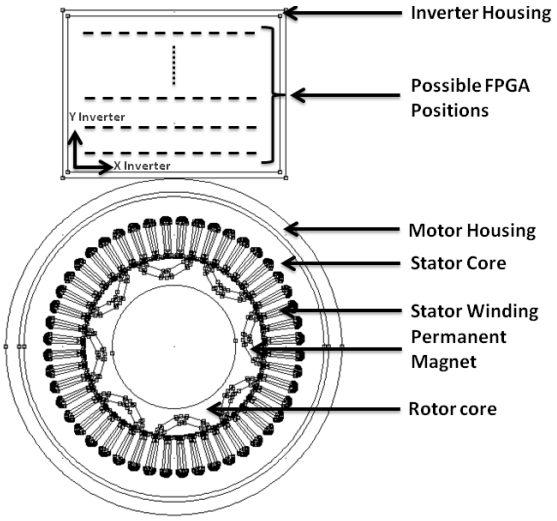

Fig. 8. 2D model of the considered electric motor and the inverter housing positioned above: the inverter relative position to the motor is dependent on vehicle integration.

and consisted in the inverter placed very close to the motor i.e. on the top of the motor. It is a common vehicle integration configuration and, for an automotive Original Equipment Manufacturer (OEM), the distance between the motor and the inverter is a parameter out of control as it is determined by the vehicle manufacturer. Fig. 8 shows the described vehicle integration in FEMM, where we considered just one millimeter between the motor housing and the inverter. The magnetic field inside the inverter has been simulated for rotor positions from 0 to 90 degrees as the motor has four pole pairs and several vertical positions, representing the possible positions of the board supporting the FPGA in the inverter.

The corresponding radiated magnetic field is given in Fig. 9 as a function of the position in the inverter at the rotor angle at which the magnetic field is maximum. Naturally, it is observed that the further away, the lower the magnetic field is, as it is inversely proportional to the distance from the field source. On another hand, Fig. 10 presents the maximal radiated magnetic

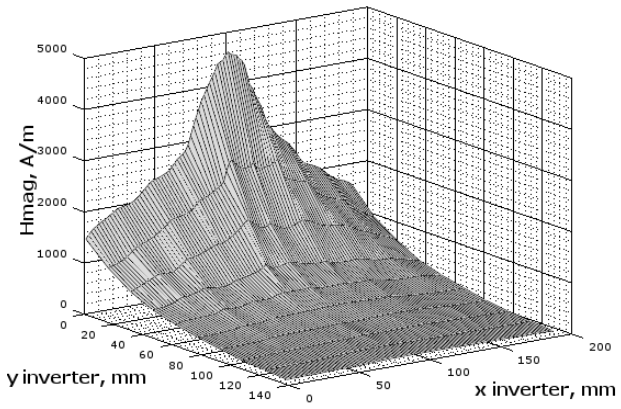

Fig. 9. Motor radiated magnetic field as a function of a position (x,y) inside the inverter.

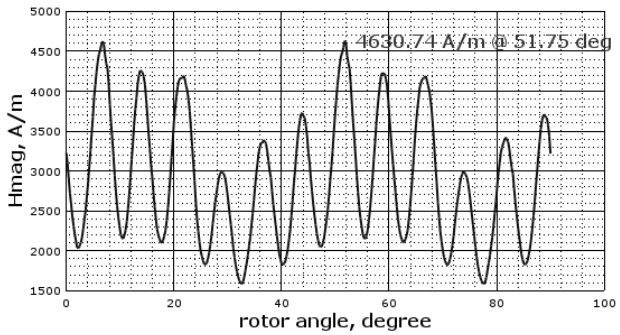

Fig. 10. Maximum Motor radiated magnetic field as a function of the rotor position.

field in the inverter geometry as a function of the rotor position. Hence we obtained a cartography of the magnetic field inside the inverter from which the corresponding effects on the FPGA can be evaluated.

C. Phase III - Effect of the Motor on the FPGA

From the first two phases of the proposed methodology, a parametric model of the FPGA sensitivity to magnetic field has been established and the magnetic field radiated from the Toyota Prius 2004 electric motor has been simulated.

An FFT of the motor magnetic field is then calculated to determine the magnetic field frequency spectrum. Only the position in the inverter at which the magnetic field is maximum has been taken into account to perform the frequency analysis in the worst case. The result is given in Fig. 11 where the shape of the magnetic field and its frequency spectrum are indicated. The FFT shows the first harmonic at approximately 80 Hz, which corresponds to the electrical frequency at motor base speed, and its following 3rd, 5th, 7th, etc. harmonics.

The frequency spectrum is then used to determine the induced voltage of the corresponding magnetic field using equation (3). This analysis has been performed for different loop surfaces from 10 mm^2 to 10 cm^2 to show the effect of the loop surface on the induced voltage and the delay variation.

For this paper, the PDN transfer function has been considered equal to one in the frequency range of interest as we are not related to a real PCB. It is nonetheless a good assumption as a real FPGA PDN would be normally designed

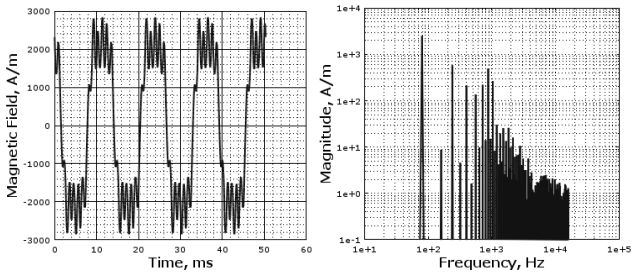

Fig. 11. Considered Magnetic Field evolution in time (left) and its FFT (right).

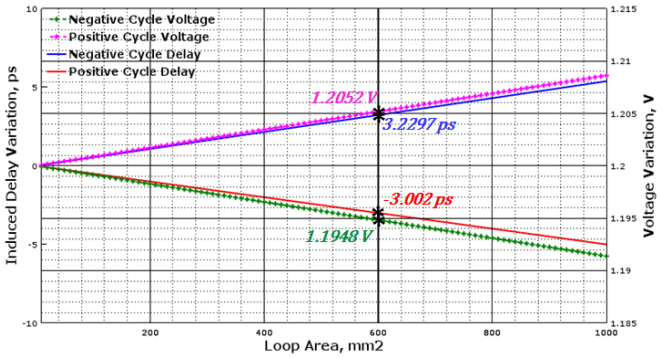

Fig. 12. FPGA Voltage variation and Delay Variation for one LUT.

to maintain a stable voltage during high-speed switching activities leading to a cut-off frequency in the range of megahertz frequencies. Hence, the induced voltage from the magnetic field coupling is directly used to compute the corresponding delay variation using the FPGA parametric model (given by equation (5)) mapping a voltage variation to its corresponding delay variation value. Fig. 12 shows the induced voltage and its corresponding delay variation for one FPGA LUT as a function of the loop area. The two patterned lines represent the voltage variations and refer to the right axis while the two solid lines representing the corresponding delay variations, refer to the left axis. As the propagation delay is inversely proportional to the voltage, the negative delay variation results from the induced voltage increasing the FPGA power supply voltage and inversely for the positive delay variation. For instance, considering a 600 mm^2 loop area, the magnetic field from the motor will cause the FPGA power supply voltage to vary from a minimum value of 1.1948 V to a maximum value of 1.2052 V. That voltage variation will induce in the same time, a delay variation from -3.002 ps when the voltage is maximum to 3.2297 ps when the voltage is minimum.

That change in the propagation delay has to be multiplied by the number of LUTs involved in the critical path. The total increase in the propagation delay of the FPGA can then induce timing faults on the FPGA depending on the slack margin of a given implemented design.

IV. Conclusion

In this paper, the influence of a high-power electric motor on an FPGA used in the drive system has been studied. This study has been done using a methodology to evaluate the effect of a magnetic field on an FPGA. According to our proposed methodology, the motor of the 2004 Toyota Prius has been modeled and simulated using finite element analysis to evaluate its stray magnetic field. Then, it has been determined how the propagation delay in the FPGA can be impacted by a magnetic field coupling on its power supply lines. By combining these two results, the effect of the motor on the FPGA is determined, regarding its relative position to the motor. Depending on the implemented design slack margin, the induced voltage can induce timing violation errors in the FPGA. Further investigations will be made in that sense to determine the effect of a magnetic field on a design implemented in an FPGA.

The Toyota Prius motor only served to explain the proposed methodology. For more powerful motors and magnetic field sources, the radiated magnetic field should be more intense and should induce a more significant delay variation.

Acknowledgment

The authors acknowledge the support of General Council of Val dOise (CGVO) and the urban community (CA) of Cergy-Pontoise, under Grant Agreement number 14RETID382 (EXELA-VO project).

References

[1] E. Monmasson and M. N. Cirstea, "Fpga design methodology for industrial control systems - a review," *IEEE Transactions on Industrial Electronics*, vol. 54, no. 4, pp. 1824–1842, Aug 2007.

[2] O. Lopez, J. Alvarez, J. Doval-Gandoy, F. D. Freijedo, A. Nogueiras, A. Lago, and C. M. Penalver, "Comparison of the fpga implementation of two multilevel space vector pwm algorithms," *IEEE Transactions on Industrial Electronics*, vol. 55, no. 4, pp. 1537–1547, April 2008.

[3] L. Idkhajine, E. Monmasson, and A. Maalouf, "Fully fpga-based sensorless control for ac drive using an extended kalman filter," in *Industrial Electronics, 2009. IECON '09. 35th Annual Conference of IEEE*, Nov 2009, pp. 2925–2930.

[4] D. Wang, K. Yu, and H. Guo, "Functional design of fpga in a brushless dc motor system based on fpga and dsp," in *Vehicle Power and Propulsion Conference, 2008. VPPC '08. IEEE*, Sept 2008, pp. 1–4.

[5] K. Miyata, K. Tsuchiya, and T. Yokoyama, "A study of 1mhz multisampling deadbeat control with disturbance compensation for pmsm drive system using fpga," in *2016 IEEE 8th International Power Electronics and Motion Control Conference (IPEMC-ECCE Asia)*, May 2016, pp. 654–659.

[6] H. Sadki, N. Coia, and B. Bouchez, "Electrical architecture for converting dc voltage into ac voltage, and vice versa," France Patent WO 2 014 128 401 A2, Aug. 28, 2014, wO Patent App. PCT/FR2014/050,340.

[7] Z. Gang, R. Yahui, D. Tongzhen, and C. Shibin, "Controller for electric vehicle motor drive system based on digital signal processor (dsp) and field programmable gate array (fpga)," China Patent CN202 696 532, Jan. 23, 2013, cN Patent 202,696,532.

[8] E. I. Boemo and S. Lopez-Buedo, "Thermal monitoring on fpgas using ring-oscillators," in *Proceedings of the 7th International Workshop on Field-Programmable Logic and Applications*, ser. FPL '97. London, UK, UK: Springer-Verlag, 1997, pp. 69–78.

[9] A. Lesea, S. Drimer, J. J. Fabula, C. Carmichael, and P. Alfke, "The rosetta experiment: atmospheric soft error rate testing in differing technology fpgas," *IEEE Transactions on Device and Materials Reliability*, vol. 5, no. 3, pp. 317–328, Sept 2005.

[10] L. Zussa, J.-M. Dutertre, J. Clediere, and A. Tria, "Power supply glitch induced faults on fpga: An in-depth analysis of the injection mechanism," in *On-Line Testing Symposium (IOLTS), 2013 IEEE 19th International*, July 2013, pp. 110–115.

[11] F. Bruguier, P. Benoit, P. Maurine, and L. Torres, "A new process characterization method for fpgas based on electromagnetic analysis," in *Field Programmable Logic and Applications (FPL), 2011 International Conference on*, Sept 2011, pp. 20–23.

[12] J. Hsu, C. Ayers, and C. Coomer, "Report on toyota prius motor design and manufacturing assessment," Oak Ridge National Laboratory (ORNL), Tech. Rep. ORNL/TM-2004/137, July 2004.

[13] J. Hsu, C. Ayers, C. Coomer, R. Wiles, S. Campbell, K. Lowe, and R. Michelhaugh, "Report on toyota prius motor torque capability, torque property, no-load back emf and mechanical losses," Oak Ridge National Laboratory (ORNL), Tech. Rep., May 2007, second Revision.

[14] A. A. Adam, S. Korolu, and K. Gulez, "Stray electromagnetic field distribution around permanent magnet synchronous motor drive," in *Industrial Electronics, 2009. IECON '09. 35th Annual Conference of IEEE*, Nov 2009, pp. 1782–1787.

[15] D. C. Meeker. Finite element method magnetics, version 4.2.